Nanoscale

Accepted Manuscript

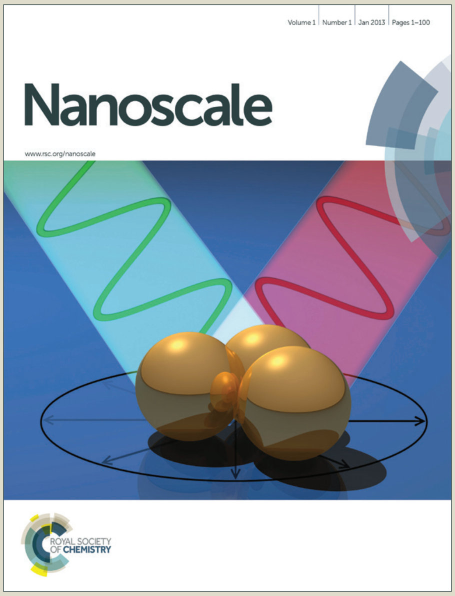

ROYAL SOCIETY OF CHEMISTRY

www.rsc.org/nanoscale

Journal Name

ARTICLE TYPE

Cite this: DOI: 10.1039/xxxxxxxxxx

Non-linear optical response by functionalized gold nanospheres: identifying design principles to maximize the molecular photo-release†

Luca Bergamini,[a,b,c,d,‡] Valerio Voliani,[e,f] Valentina Cappello,[e] Riccardo Nifosì,[g] and Stefano Corni[a,‡]

Received Date
Accepted Date

DOI: 10.1039/xxxxxxxxxx

www.rsc.org/journalname

In a recent study by Voliani *et al.* [Small, 2011, **7**, 3271], the electromagnetic field enhancement in the vicinity of gold nanoparticle surface has been exploited to achieve photocontrolled release of a molecular cargo conjugated to the nanoparticle *via* 1,2,3-triazole, a photocleavable moiety. The aim of the present study is to investigate the mechanism of the photorelease by characterizing the nanoparticle aggregation status within the cells and simulating the electric field enhancement in a range of experimentally realistic geometries, such as single Au nanoparticles, dimers, trimers and random aggregates. Two plasmon-enhanced processes are examined for triazole photocleavage, i.e., three-photon excitation and third-harmonic-generation (one-photon) excitation. Taking into account the absorption cross sections of triazole, we conclude that the latter mechanism is more efficient, and provides a photocleavage rate that explains the experimental findings. Moreover, we determine which aggregate geometries are required to maximize the field enhancement, and the dependence of such enhancement on the excitation wavelength. Our results provide design principles for maximizing the multiphoton molecular photorelease by such functionalized gold nanoparticles.

Keywords: Plasmon, nanoparticle, three photon, third harmonic, triazole

1 Introduction

Recently, functionalized nanoparticles (NPs) have demonstrated a clear potential for drug delivery[1–3]. On one hand, by exploiting proper functionalization on their periphery, they can be directed to a specific target where the drug should be delivered, maximizing the therapeutics efficiency by minimizing side effects[4–6]. On the other hand, nanoparticles can also have an active role in the drug release, being able to transduce an external stimulus (e.g., light) in the liberation of a payload and thus in its “on demand” bioavailability at a specific time and location[7,8]. This is achieved by exploiting the plasmonic excitation of the metal NPs, i.e. the effects of the collective coherent excitations of the conductive electrons taking place at specific frequencies in the Vis-NIR[9,10]. A proof of principle that such a remotely-controlled delivery is possible has been previously given using gold nanoparticles functionalized with a peptide spacer connected by click-chemistry to a payload via a photolabile moiety[11,12]. In particular, the experimental data indicated that payload delivery through photodissociation involves a non-linear excitation process promoted by the plasmonic gold nanoparticle.

In such a system, the NPs are covered by an organic moiety (peptides) bridging the payload and the particle surface (as sketched in Figure 1). The connection between the peptide and

---

[a] Centro S3, CNR Istituto Nanoscienze, Via Campi 213/A, 41125 Modena, Italy.
[b] Dipartimento di Scienze Fisiche, Informatiche e Matematiche, Università di Modena e Reggio Emilia, Via Campi 213/A, 41125 Modena, Italy. E-mail: stefano.corni@nano.cnr.it
[c] Department of Electricity and Electronics, Faculty of Science and Technology, UPV/EHU, Barrio Sarriena s/n, 48940 Bilbao, Vizcaya, Spain.
[d] Materials Physics Center CSIC-UPV/EHU and Donostia International Physics Center DIPC, Paseo de Manuel Lardizabal 5, 20018 San Sebastián, Spain. E-mail: luca.bergamini@ehu.eus
[e] Center for Nanotechnology Innovation@NEST, Istituto Italiano di Tecnologia, Piazza San Silvestro 12, 56127 Pisa, Italy.
[f] NEST - Scuola Normale Superiore, Piazza dei Cavalieri 7, 56126 Pisa, Italy.
[g] NEST, Istituto Nanoscienze-CNR, Piazza San Silvestro 12, 56127 Pisa, Italy.

† Electronic Supplementary Information (ESI) available: ESI material includes some complementary figures on the study of the 3PE intensity enhancement around single and coupled nanoparticles. Moreover, a comparison with analytical results (Section “Comparison with analytical benchmarks”), a study of the retarded effects (Section “Retarded vs. Quasi-Static”), a verification of the validity of the NP surface discretization used for BEM simulations (Section “Test over the tessera number”) and details of the analyzed aggregation configurations (Section “Aggregate configurations”) are also provided. See DOI: 10.1039/b000000x/

‡ To whom the correspondence should be addressed.

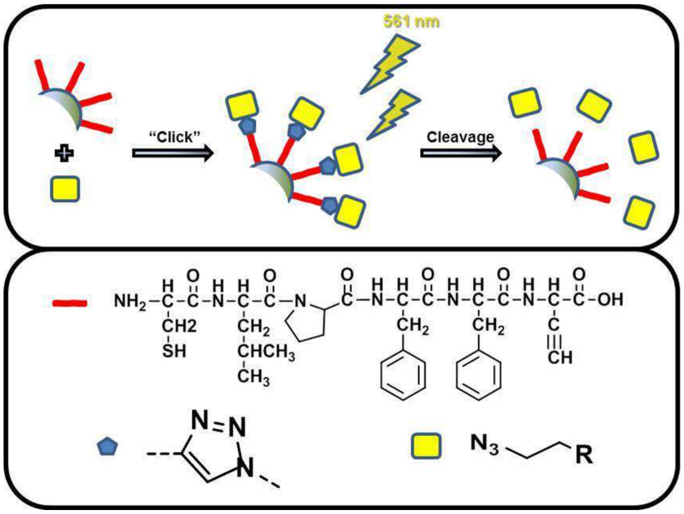

Fig. 1 Out of scale schematic picture of the click-chemistry conjugation and 561nm photorelease. On the left, the click-chemistry reaction with the peptide-encapsulated nanostructure (water-synthesized gold nanoparticles, in green, and hexa-peptide CLPFF-propargylglycine, in red) and the azide-modified payload, yellow square. On the right, the photocleavage process induced by low-power irradiation at 561 nm of the 1,2,3-triazolic ring (in blue) and subsequent release of the payload. For the sake of simplicity the modifications of peptide and payload induced by the reactions are not shown.

the payload is accomplished by means of click-chemistry via a 1,2,3-triazole photocleavable unit. 1,2,3-triazole is known to undergo fast photochemical decomposition upon irradiation in the far UV (at 190nm)[13]. Experimentally, release of the cargo, implying cleavage of the peptide-payload bond, is observed when the system is irradiated at the wavelength of 561nm. This behavior along with the observed cubic dependence of the release rate upon irradiation intensity suggested a three-photon excitation (3PE) process as the mechanism of photodissociation[14]. To enable such a low-probability process at the intensity associated with the incident laser beam, electromagnetic (EM) field enhancement should occur, provided by the gold nanoparticles resonating at the plasmon wavelength. The parameters of the experimental apparatus suggested that an enhancement of around ten order of magnitude is required for this process to be relevant, namely $(I_T^{3PE})^3 \approx 10^{10}(I_T^{inc})^3$, where I_T^{inc} is the EM field intensity of the incident laser beam (the derivation is detailed in the Electronic Supplementary Information of Ref.[11] and expanded here). Note that this value implies an enhancement of the electric field around 50, which is not unreasonable in light of literature results[15–25].

Besides that, it is well-known that irradiating a gold NP at the plasmon wavelength not only results in a strong enhancement of the linear optical properties of the NP, e.g., the extinction cross section and the linear EM near-field[26,27], but also increases the non-linear response of the metal NPs, such as Second and Third Harmonic Generation (SHG and THG)[28,29]. In particular the plasmon-enhanced conversion of three photons with frequency ω into one photon with frequency 3ω (THG)[30–32] may supply photons of suitable wavelength (around 190nm) for exciting the triazole moiety, thus competing with the three-photon absorption process, and also resulting in a cubic dependence on the irradiation intensity. Similarly to the 3PE case, to make this process relevant an enhancement of the incident EM field is required, and in particular such that the ratio $I^{THG}/(I^{inc})^3$ is larger than a threshold derived here.

The present work aims at investigating the effectiveness of these two excitation mechanisms - 3PE and THG - in experimentally realistic conditions. Indeed, the EM field close to the NP is affected by the presence of other NPs, which can either hinder or foster the near-field enhancement depending on the configuration of the aggregate[25,33–35]. Hence, local hot spots could appear in the gap of strongly coupled NP aggregates or near the sharp tip of non-spherical nanoparticles[12,26,36]. The role of these so-called "plasmonic hot-spots" has been identified as the main cause of local EM field enhancement, exploited in particular in Surface Enhanced Raman Scattering (SERS) applications. Thus, we simulated the EM field around isolated NPs and various aggregates of NPs in order to identify favorable NPs configurations in relation to the payload photorelease. Since the near-field enhancement decreases rapidly by increasing the distance from the nanoparticle surface, molecular dynamics (MD) simulations were also performed to determine the thickness of the peptide spacer and, in turn, the distance between the photocleavable bond and the NP surface. The latter turns out to be around 1-2nm, so that we focused on the electric field enhancement at this distance from the NP surface, for both investigated processes. We have first analyzed 3PE, for which we generally found enhancements only barely sufficient to justify photorelease in the experimental conditions. Because of that, for 3PE we have considered a large variety of NP arrangements, all compatible with experimental evidences, to search as extensively as possible for the highest possible 3PE rate. For THG, we found that NP dimers are sufficient to yield an excitation rate in line with the experimental results, and, based also on 3PE results, we stopped our search at this level. In both cases, the synergy among interacting NPs turns out to be essential to generate hot-spots promoting an amount of photorelease in agreement with the experiments.

2 Theory

Upon irradiation at the plasmonic peak (561nm for the system considered here), the optical response of the gold NP may induce photodegradation of the triazole moiety by two mechanisms, both compatible with the observed cubic dependence on irradiation power: i) three-photon excitation (3PE), at a wavelength of 561nm, due to the enhanced (linear) electric field (which leads to the three-photon absorption) and/or ii) one-photon excitation (1PE), at a wavelength of 187nm, due to generation of photons of threefold fundamental frequency (third harmonic generation). Assuming orientational averaging, the excitation rates of the two mechanisms, k^{3PE} and k^{THG}, respectively, depend on the intensity of the NP optical responses at the NP surface (I^{3PE} and I^{THG}) and on the cross sections of triazole for the two excitation processes,

σ_{3PE}^{561} and σ_{1PE}^{187}, by the following relations

$$k^{3PE} = \frac{1}{3}\sigma_{3PE}^{561}\left(\frac{I^{3PE}}{h\nu^{inc}}\right)^3 = \frac{\sigma_{3PE}^{561}}{3}\left(\frac{I^{inc}}{h\nu^{inc}}\right)^3\zeta \qquad (1)$$

$$k^{THG} = \sigma_{1PE}^{187}\left(\frac{I^{THG}}{3h\nu^{inc}}\right) = \sigma_{1PE}^{187}\frac{I^{inc^3}}{3h\nu^{inc}}\eta \qquad (2)$$

where ν^{inc} is the frequency of the impinging photon, such that $I/h\nu^{inc}$ gives the photon number, $\zeta = (I^{3PE}/I^{inc})^3$, the intensity enhancement factor, and $\eta = I^{THG}/(I^{inc})^3$, the THG efficiency, relate the linear and THG response of the NP to the incident laser intensity I^{inc}. B3LYP 6-31+G(d) time-dependent density functional calculations detailed in ref. [11] yield the results reported in Table 1 for the first 4 excitations of 1,2-methyl-3-triazole (the two methyl groups are added to account for the connections to the peptide on one side and the payload on the other, see Figure 1). Note that the oscillator strength of ≈ 0.1 of excitation 2 is in agreement with configuration interactions calculations on 1,2,3-triazole yielding an o.s. of 0.13 for the excitation at 5.93eV[37].

Using an irradiation wavelength of 561nm gives $h\nu^{inc} = 3.54 \cdot 10^{-19}$J. Typical experimental intensities are in the range $0.47 \cdot 10^9$W/m^2 to $1.3 \cdot 10^9$W/m^2 (considering an irradiation power of $70-200\mu$W and irradiated area of 0.15μm^2). The one and three-photon cross sections of the 3rd excitation (closest to 187nm) are $\sigma_{3PE}^{561} = 0.36 \cdot 10^{-92}$m^{6}s^2 (for linearly polarized light) and $\sigma_{1PE}^{187} = 0.5 \cdot 10^{-19}$m^2. We note that the cross sections at 205nm are larger both for 1PE and 3PE, so that structures with plasmon resonance at $\approx 205\text{nm} \cdot 3 = 615\text{nm}$ would result in more efficient photorelease at that wavelength.

The quantum yield of 1,2,3-triazole photodegradation is not known precisely, but values not much smaller than one are reasonable in line with the high reported photolability of the molecule[13]. Thereby, we expect that upon absorption a sizable fraction of triazole will undergo photodissociation and consequent payload release, and thus k^{3PE} and k^{THG} are good estimates of the total photorelease rates resulting from each process. This consideration and the values of the constants given above indicate that non-negligible excitations rates ($> 10^{-2}$ s^{-1}) are expected for $\zeta > 10^{10}$ and $\eta > 10^{-25}$m^{4}W^{-2}, respectively for the 3PE and THG processes. The theoretical/computational estimation of these factors for realistic system configurations, *via* EM field simulations, is the focus of the present work.

The EM fields are calculated by solving the Maxwell equations in media described by homogeneous and isotropic dielectric functions, enforcing the relevant matching conditions at medium interfaces (see Methods). Figure 2 shows a single gold nanosphere with frequency dependent dielectric function $\tilde{\varepsilon}$ embedded in a non dissipative medium with $\tilde{\varepsilon}_M$. The external perturbation is described by a monochromatic EM plane-wave, with linear polarization on the x-axis and propagating along z, its electric field given by $\vec{E}^{inc} = \vec{E}_0(e^{i\omega t} + c.c.)$. The linear response electric field $\vec{E}_{tot}(\vec{r},t)$ is the superimposition of the incident and scattered field outside the nanoparticles. The 3PE enhancement ζ is calculated locally as $(I_T^{3PE}/I_T^{inc})^3$, where I_T^{3PE} is the local linear EM field intensity averaged over time, i.e.,

$$I_T^{3PE}(\vec{r}) = \sqrt{\frac{\tilde{\varepsilon}}{\tilde{\mu}}}\langle\left|\vec{E}_{tot}(\vec{r},t)\right|^2\rangle_T = \sqrt{\frac{\tilde{\varepsilon}}{\tilde{\mu}}}\frac{1}{T}\int_0^T\left|\vec{E}_{tot}(\vec{r},t)\right|^2 dt \qquad (3)$$

where $\tilde{\varepsilon}$ and $\tilde{\mu}$ are the permittivity and permeability, respectively, of the medium in which the intensity is to be calculated. The other time-averaged intensities are calculated analogously. $\vec{E}_{tot}$ is assumed to be representative of the local field felt by the molecules close to the NP surface. A more accurate model should include the presence of such molecules since they may affect the optical properties of the resonant nanoparticle. However, we do not expect this approximation to significantly change the EM field[38]. The peptide moiety is commonly simulated as non-dissipative matter with refractive index equal to $n_p = 1.4$[39], so that the difference in refractive index between the molecules and the embedding water ($n_w = 1.33$) is small. As showed in the Electronic Supplementary Information, the presence of a molecule-coating does not change the magnitude of the field remarkably, the 3PE enhancement factor ζ changing by less than 10%.

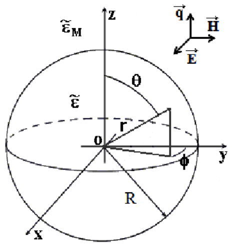

Fig. 2 Sketch of the model nanoparticle. The wave vector of the incident radiation is set to be along the z-axis, whereas the incident electric filed is along the x-axis

Whereas the three-photon excitation process depends on the linear optical response of the NP (and on the non-linear absorption by triazole), non-linear contributions of the material, such as second and third harmonic generation, may become relevant for high enough field strengths[28,29]. The plasmon resonance is known to enhance the rate of both SHG and THG[30,32,40]. Nevertheless, a SHG field at doubled frequency (namely at a wavelength around 280nm) is not relevant in our case because the triazole does not exhibit an absorption for such a frequency[37]. In contrast, THG radiation at tripled frequency (i.e., at wavelength around 190nm) might be absorbed by the molecule and contribute to the photodissociation since the fundamental absorption frequency of the molecule resides in such a range[37]. The experimentally determined dependence of the photorelease on the third power of the incident intensity can also be explained by metal THG. To check the influence of this non-linear contribution we calculated the electric field produced by the THG process in an isolated NP and NP dimer. According to Ciracì et. al[41], this THG contribution arises from a bulk response of the material and for an isotropic medium it originates a polarization inside the material itself which reads

$$\vec{P}^{THG}(\vec{r},3\omega) = \varepsilon_0\chi_{3\omega}^{(3)}\left(\vec{E}\cdot\vec{E}\right)\vec{E} \qquad (4)$$

n.	energy (eV)	wavelength (nm)	o.s.	δ^L_{3PE} (a.u.)	δ^C_{3PE} (a.u.)	σ_{1PE} $10^{-19}\mathrm{m}^2$	σ^L_{3PE} $10^{-92}\mathrm{m}^6\mathrm{s}^2$	σ^C_{3PE} $10^{-92}\mathrm{m}^6\mathrm{s}^2$
1	5.65	219.5	$5.4 \cdot 10^{-3}$	$4.3 \cdot 10^{2}$	$5.8 \cdot 10^{1}$	0.38	$2.2 \cdot 10^{-4}$	$2.9 \cdot 10^{-5}$
2	6.03	205.5	$1.1 \cdot 10^{-1}$	$3.8 \cdot 10^{5}$	$7.3 \cdot 10^{5}$	7.44	$8.5 \cdot 10^{-1}$	$4.4\ 10^{-1}$
3	6.55	189.5	$7.2 \cdot 10^{-3}$	$4.6 \cdot 10^{5}$	$8.8 \cdot 10^{5}$	0.50	$3.6 \cdot 10^{-1}$	$6.8 \cdot 10^{-1}$
4	6.80	182.5	$2.3 \cdot 10^{-2}$	$3.5 \cdot 10^{6}$	$1.5 \cdot 10^{5}$	1.55	$3.1 \cdot 10^{-3}$	$1.3 \cdot 10^{-3}$

Table 1 Excitation energies, oscillator strengths (o.s.), 3PE momenta (δ^L_{3PE}, δ^C_{3PE}, with L and C referring to linearly and circularly polarized light, respectively), one and three photon cross sections (σ_{1PE}, σ^L_{3PE}, σ^C_{3PE}). The cross sections are calculated assuming a lorenzian linewidth of 0.1eV.

where ε_0 is the electric permittivity *in vacuo*, $\vec{E}$ is the electric field inside the NP and $\chi^{(3)} = \chi^{(3)}_{3\omega}$ reduces to a scalar. Boyd et al.[42] compare measurements of this quantity made via different experimental methods. The susceptibility $\chi^{(3)}_{3\omega}$ seems to be slightly dependent on the frequency but largely affected by the duration of the exciting impulse. The tabulated values span from $7.7 \cdot 10^{-19}\mathrm{m}^2/\mathrm{V}^2$ to $6.22 \cdot 10^{-14}\mathrm{m}^2/\mathrm{V}^2$. We made a conservative choice of $2.3 \cdot 10^{-18}\mathrm{m}^2/\mathrm{V}^2$, the value suggested in the Boyd's book[28] for bulk gold.

To a first approximation[43] the relative weight of the THG term is determined by the strength of the incident EM field as compared to the atomic field, i.e., $(E_{inc}/E_{atom})^2$. From $I^{inc} \approx 0.47 - 1.3 \cdot 10^9 \frac{W}{m^2}$, the incident electric field amplitude is obtained from the relation

$$E_{inc} = \sqrt{I^{inc} Z_0} \approx 4.2 - 7 \cdot 10^5 V/m \tag{5}$$

where $Z_0 = \sqrt{\mu_0/\varepsilon_0} \approx 377\Omega$ is the impedance of free space (μ_o is the magnetic permeability *in vacuo*). The typical value for the atomic electric field is $E_{atom} \approx 10^{10} V/m$[43]. Thereby, the THG contribution is treated as a perturbation, and we substitute the electric field appearing in formulas (4) with that yielded by considering only the linear contribution.

The bulk polarization vector $\vec{P}^{THG}$ represents the dipole moment per volume unit induced inside the NP by the THG process. The THG electric field is, thus, the superimposition of the electric field originated by all these induced dipoles, viz.

$$\vec{E}^{THG}(\vec{r},\omega) = \int_V \frac{\left[\vec{P}^{THG} \cdot (\vec{r}-\vec{r}\,')\right] \cdot (\vec{r}-\vec{r}\,')}{4\pi\varepsilon_0 |\vec{r}-\vec{r}\,'|^5} - \frac{3\vec{P}^{THG}}{4\pi\varepsilon_0 |\vec{r}-\vec{r}\,'|^3} d\vec{r}\,' \tag{6}$$

where V is the NP volume, $\vec{r}$ and $\vec{r}\,'$ indicates a point outside and inside the particle, respectively. The numerical procedure used for obtaining $\vec{P}^{THG}$ and performing the numerical volume integration are described in Section "Electromagnetic simulations".

To estimate in which position the chromophore resides, namely in which position to calculate the enhanced intensities, we also performed atomistic molecular dynamics (MD) simulations of the peptide adsorbed on the gold nanoparticles surface. In the absence of detailed experimental characterization, MD affords a plausible picture of the structural properties of the system by taking account molecular and NP-molecule interactions. The details are given in the next section.

3 Methods and computational details

3.1 Molecular dynamics simulations

We performed molecular dynamics simulations of the 5 a.a. peptides anchored to Au(111) surface. The sequence of the simulated peptide is Cys-Leu-Pro-Phe-Phe-Ala (CLPFFA), i.e., the same as in the experimental setup, apart from the last amino acid. The choice of an Alanine in this position was suggested by the lack of force field parameterization of the triazole ring. The CB atom of Alanine is in the equivalent position of one of the two carbon atoms in the ring. Hence, its distance from the gold surface is a good indicator of triazole-Au distance, the estimate of which is the purpose of the MD simulations. A slab of twelve $\approx 5.7\mathrm{x}4.4\mathrm{nm}^2$ gold layers represented the Au(111) surface, and 3D periodic boundary conditions were applied, leaving a 7.9nm z-distance between periodic images of the gold slab.

The simulations were performed using the OPLS/AA force field combined with the GolP force field[44] for describing Au-protein interactions. The system was solvated in SPC water molecules.

The thiol-Au covalent bond is not described by the GolP force field. As a consequence, the anchoring of the peptides to the Au surface was accounted for by adding a $5000\mathrm{kJ/mol/nm}^2$ harmonic restraint on the distance of the CYS sulfur atom from the surface.

The simulations were performed with the GROMACS 4.5 code[45] in the NVT ensemble, using the Nosé-Hoover thermostat[46] with a coupling constant of 0.4ps. All bond lengths were constrained with the SETTLE algorithm[47].

Since no structural information on the peptide arrangement on the surface is available, we opted for an unbiased description of the self assembly process, in which the peptides are randomly placed in the solution and forced to interact with one side of the gold slab by an increasing harmonic restraint on the Au-sulfur atom distance.

Two systems were simulated, containing 24 or 40 peptides (see Figure 3). While few peptides are easily anchored to the gold surface, when a larger number is present, the anchoring may be hampered by the crowding of the other peptides. In these cases high (400K) temperature MD simulations were performed to accelerate the configurational sampling and allow for a larger number of peptides to anchor the Au surface.

After the preparation phase, the production runs were performed for 0.5μsec.

3.2 Electromagnetic simulations

To simulate the EM field around NPs subject to an EM radiation we used the Boundary Element Method (BEM)[48]. This method

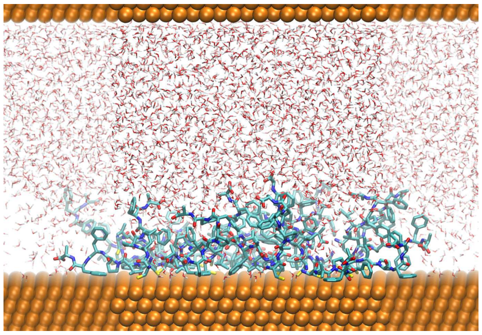

Fig. 3 Simulated system, containing 24 CLPFFA peptides and water molecules (shown in licorice representation, with usual coloring code for atoms) and the AU slab (shown as VdW spheres in orange). Periodic images of the water molecules and of the Au slab are shown in transparent mode on the left and right sides.

leans on the solution of the Maxwell equations with EM field matching at medium interfaces (boundary conditions). In short, this method includes a 2-steps solving-process: first, the EM field is expressed in terms of fictitious charges and currents at the medium interfaces, and the integral equations determining such quantities are written to satisfy boundary conditions; second, by means of a discretization of the interface surfaces, the solution of the integral Maxwell equations is transformed in the solution of a self-consistent system of linear equations. In practice, we exploited the Matlab toolbox MNPBEM by Hohenester and Trügler[49], which implements the formalism developed by Garcìa de Abajo and Howie[50].

The systems under investigation with this method include one-, two- and three-NP configurations. The NPs are assumed to be spheres with a radius (R) of 15nm impinged by a plane wave with wavelength equal to 561nm. Although the simulation of non-regularly shaped NPs is feasible with the MNPBEM toolbox, only spherical nanoparticles were accounted for, their shape being closer to the experimental one. A gold dielectric function, interpolated from experimental data by Johnson and Christy[51], was employed to reproduce the optical properties of the NPs, whereas the water dielectric constant ($\tilde{\varepsilon}_M = 1.77$) was chosen to represent the embedding solution. The NP surface was discretized in 2884 triangular pieces (called tesserae in the following): this number is the largest provided by the toolbox for a tessellation of equilateral triangles (corresponding to the sphere-commensurate number of 1444 vertices). Tests performed with different discretizations showed that the chosen number of tesserae gives rise to reliable results (see Section "Test over the tessera number" in the Electronic Supplementary Information, ESI, for more details). Furthermore, we compared the results for a single NP with the output by an in-house Fortran implementation based on the Mie theory[52]. The test reveals that the MNPBEM calculations are qualitatively and quantitatively in agreement with the benchmark (we refer to Section "Comparison with analytical benchmarks" in the ESI for further discussion).

Finally, note that we study this system in the retarded framework. Indeed, as the simulations were not prohibitively time-consuming, we decided to exploit the retarded approach even if the quasi-static outcomes are very close to retarded ones. Mainly, the former is found to slightly underestimate the latter and to have a different plasmon dephasing with respect to the incident radiation (see Section "Retarded vs. Quasi-Static" in the ESI for more details).

The same MNPBEM toolbox was also exploited to calculate the electric field produced by a THG process. This calculation requires the knowledge of the electric field inside the NPs which was computed on a uniform 1-nm paced cartesian grid (convergence tests were performed and confirmed this value as providing reliable results). Subsequently, we treated these points as dipole sources endowed with a dipole moment proportional to the third power of the obtained inner electric field according to Equation (4). Hence, we extracted the electric field produced by this set of dipoles on a 0.1-nm paced grid of points outside the spheres (the closest outer points have a distance from the surface of 0.1nm). By means of this last step, corresponding to a numerical integration over the NPs volume of the THG dipoles, we obtained the electric field by third harmonic generation.

The necessity of discretizing the NP surface finely and the significant rise of the simulation time-demand at increasing tessera numbers makes the BEM inadequate to simulate aggregates even of a few tens of NPs. For this reason, we employed the Coupled Dipole Approximation (CDA) for the calculation on aggregates[53]. In this method each NP is seen as a dipole characterized by a scalar, complex polarizability ($\tilde{\alpha}$) and subject to the incident external field as well as the scattered field generated by the other NPs. As a result, a self-consistent equation system is set up whose solution provides the polarization ($\vec{P}$) of each NP which can be used to infer other optical properties (e.g., extinction cross section). The interaction among NPs includes retarded terms of the electric fields, even if only the dipolar response is accounted for. The polarizability is taken from the retarded Mie solution for sphere. Since this method assumes that the polarization is the NP response to the local electric field, we considered $\vec{E} = \vec{P}/\tilde{\alpha}$ to be representative of the NP near-field. In practice, we exploited the seminal Fortran implementation by Draine and Flatau[54]. The aggregates were created thanks to a Fortran code developed by one of us[55]. This implementation is based on the Cluster-Cluster Aggregation (CCA) model[56], which, starting from a random NP distribution, moves randomly the NPs and the NP clusters that are originated when the NPs come into contact and stick together irreversibly. The process ends when only a single cluster is present. The initial distribution as well as the motion is performed on a cubic lattice: specifically, a grid with an internode distance of 11nm was used to build-up differently shaped aggregates of around 50 NPs.

3.3 TEM imaging

U2Os cells were fixed as monolayer (with a solution of 2% glutaraldehyde in cacodylate buffer) then scraped and centrifuged to obtain a stable pellet. Pellets were fixed in the same fixative solution over night and processed with a standard embedding protocol (as previously shown by Del Turco et al.[57]). Cells were washed in cacodylate buffer, then postfixed with osmium tetroxide 2% in the same buffer, then dehydrated with ethanol growing series and embedded in epoxy resin. After resin polymerization (48 hours, 60°C) samples were cut in thin sections (80-90nm). Sections were collected over 300 mesh copper grids and were analyzed using a Zeiss Libra 120 Plus transmission electron microscope operating at 120kV and equipped with an in-column omega filter and 16-bit CCD camera 2k x 2k bottom mounted.

4 Results and discussion

4.1 Triazole-Au surface distance from MD simulations

Molecular dynamics simulations were performed to provide an estimate of the average triazole-Au surface distance. The two simulated systems consist of 24 and 40 CLPFFA peptides bound to a planar $5.7 \cdot 4.4 \mathrm{nm}^2$ slab of gold, 2.6nm thick, with 3D periodic boundary conditions. On the scale of the 30nm diameter sphere, the deviation from planarity of the simulated portion amounts to less than 0.01nm. Experimental estimates of peptide number per AuNP vary from 750 to 4000 depending on the system production process[11]. These values correspond to, respectively, 7 and 35 peptides in the simulated portion, so that our simulated systems are close to these ranges. Figure 4 reports the distribution of the distance between the AU surface and the β-carbon (CB) atom of the C-terminal Alanine. The latter is in a position analogous to one of the carbon atoms of triazole (see Methods). The average distance is 1.05 ± 0.42nm and 1.17 ± 0.58nm for the 24 and 40 peptide systems, respectively. In both graphs, there is a peak at around 0.25nm, indicating a significant amount of C-terminal Alanine very close to the AuNP surface. The contribution of such molecules is neglected because of the quenching effect due to the proximity to the Au surface[58] and because such an arrangement is not realistic considering the presence of the payload attached to triazole. To conclude, we took 1nm as representative of the most significant distance (d) between the photocleavable bond and the AuNP surface and we investigated the EM field enhancement at this distance.

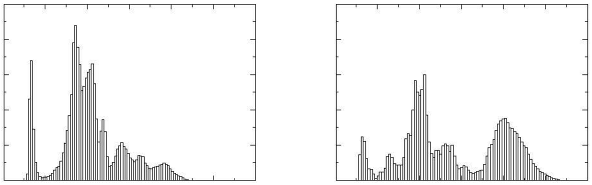

Fig. 4 Distribution of the distance between the ALA CB atom and the Au surface during the 0.5μs MD simulations, in the systems with (left) 24 and (right) 40 peptides.

4.2 The EM field enhancement in Au-NP geometries relevant within cells

Figure 5 shows TEM images of fixed U2Os cells after uptake of the peptide-coated AuNs. The images reveal that the Au-NPs can be found as isolated NPs or arranged in dimer or trimer configurations. Aggregates are also present: some of them are more compact with transverse size up to a few hundreds of nanometers (cfr. Figure 5a), whereas others are more diluted and elongated (cfr. Figure 5b).

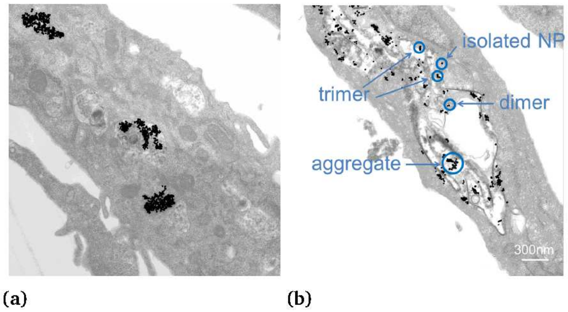

Fig. 5 TEM images of two samples showing the arrangements of the functionalized Au-NPs inside human osteosarcoma cells. The circles mark off the various arrangements.

Based on these results, we decided to consider different kinds of NP aggregates in our simulations, namely single gold NP, dimers of NPs, trimers of NPs (linear and arranged as a square triangle) and random aggregates of different compactness.

4.2.1 Electromagnetic field enhancement around an isolated nanoparticle

The isolated NP was placed in the center of a polar coordinate system (r,θ,ϕ) and a spherical grid, whose nodes identify the points in which the electric field is to be evaluated, was built-up all around the nanoparticle. Figure 6a shows how the electric field appears when the plasmon is excited (normalized by the incident electric field amplitude $|\vec{E}_0|$). The arrows represent the electric field direction and versus, whilst their size and color are directly proportional to its magnitude.

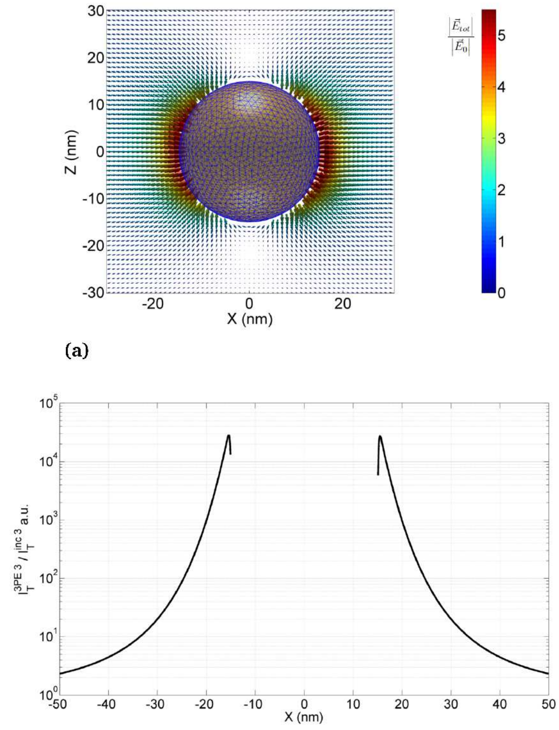

(a)

(b)

Fig. 6 Total electric field ($\vec{E}_{tot}$) and EM field intensity outside the NP. Panel (a): xz view of the electric field. The color scale and the size of the arrows represent the module of the field in unit of the incident field module ($|\vec{E}_0|$). Panel (b): Third power of the total EM field intensity along the x-direction. The missing part in the plot corresponds to the region internal to the NP.

Looking at this figure we can state that a 561nm wavelength EM radiation impinging a 15-nm radius gold nanoparticle essentially produces a dipole induced electric field whose effects extend up to about 10nm from the nanoparticle surface. Both the spatial distribution and the obtained range of the electric field enhancement agree with benchmarking results in the literature[9,52,59].

The 3PE enhancement factor $\zeta = (I_T^{3PE}/I_T^{inc})^3$ averaged over the solid angle (showed in Figure S1 of the ESI) at the relevant distance $d = 1$nm is $\simeq 600$, and rapidly decreasing in a 10nm range, i.e., several order of magnitude below the estimated threshold (10^{10}) for relevant three-photon excitation process. Locally, the maximum enhancement takes place at the poles on the electric field polarization direction, namely the x-axis. A scan along this direction is plotted in Figure 6b, revealing values of ζ below 10^5, i.e., still insufficient to trigger 3PE. Note that the electric field tends to decrease very near (a few Å) the nanoparticle surface, namely for values close to -15nm and 15nm: this is an artifact due to discretization.

Finally, for the sake of completeness, we simulate the EM field enhancement occurring when the NP is covered by a 2nm thick shell with permittivity equal to 2. Such a shell is taken representative of the layer formed by the peptides and spacing the payload from the AuNP surface[39]. The results, showed in Figure S3 of the ESI, reveal that the magnitude of the enhancement is not modified by the presence of molecules significantly.

4.2.2 Electromagnetic field enhancement around coupled nanoparticles

The mutual interaction between two nanoparticles significantly affects the plasmonic properties[16,19–22,60]. The greatest EM field enhancement is known to take place when the NPs are aligned along the electric field direction[15,17,18,23,24]. Therefore, we simulated two identical gold nanoparticles, with a surface distance D, arranged along the plane-wave polarization direction. $\vec{E}_{tot}$ around the nanoparticles is reported at D =3nm (Figure 7a) and D =45nm (Figure 7c), together with 3PE enhancement factor along the x-direction.

The obtained electric field enhancement values and distribution around the nanoparticles are in agreement with other studies revealing electric-field focusing in the intervening region of the dimer, with enhancement factors on I also larger than 10^2, such as for nanoparticle and nanowire dimers[15–25]. As expected, the maximum values of the electric field are along the x-direction. When the NPs are close ($D = 3$nm) a hot-spot is created, i.e. there is a great EM field enhancement between the nanoparticles, whereas at increasing separation the effect vanishes and the values approach those of an isolated nanoparticle. The complete behavior of η x-scans at varying D is reported in Figure S3. At the hot-spot the EM field enhancement seems sufficient to trigger the three-photon process, according to the estimated threshold ($\eta \approx 10^{10}$), only when $D \approx 3$nm, namely when the NPs are in contact to each other via the peptide coating. This type of configuration is reasonable in light of the MD simulations, which reveal that the peptides form a layer slightly thicker than 1nm around the NPs.

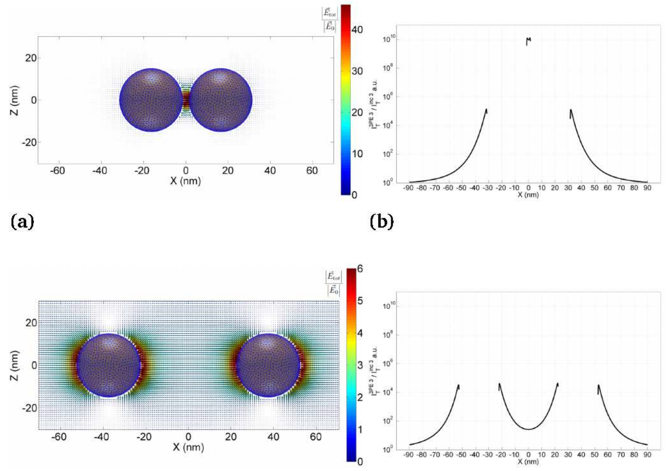

(a) (b)

(c) (d)

Fig. 7 Total electric field ($\vec{E}_{tot}$) and EM field intensity outside the NPs. Panels (a) and (c): xz views of the electric field for (a) $D = 3$nm and (c) $D = 45$nm. The colorscale (different for the two panels) and the size of the arrows represent the module of the field in unit of the incident field module ($|\vec{E}_0|$). Panels (b) and (d): Third power of the total EM field intensity along the x-direction for the two distances. The missing parts in the plot correspond to the regions internal to the NPs.

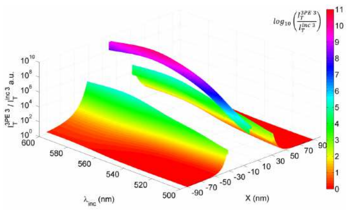

Fig. 8 Third power of the total EM field intensity along the x-direction for varying incident wavelength in a system of coupled NPs separated by 3nm. The missing parts in the plots correspond to the regions internal to the NPs.

To verify whether the enhancement value is already optimized with respect to the light frequency in such a configuration, we calculated the EM field intensity as a function of the incident wavelength for a pair of NPs separated by 3nm. The curve (Figure 8) shows that an incident radiation with $\lambda = 569$nm theoretically provides the greatest enhancement. This value confirms the validity of the experimental wavelength and the agreement between simulations and experimental findings.

Finally, note that the classical description used here is tenable till the nanoparticle distance is of a few Å: as a matter of fact, for subnanometric interparticle separation non-local and quantum effect are proved to be significant, so that a quantum mechanical description or a corrected classical electromagnetic theory must be adopted[16,18,20–22,24,61,62].

4.2.3 Electromagnetic field enhancement around trimer of nanoparticles

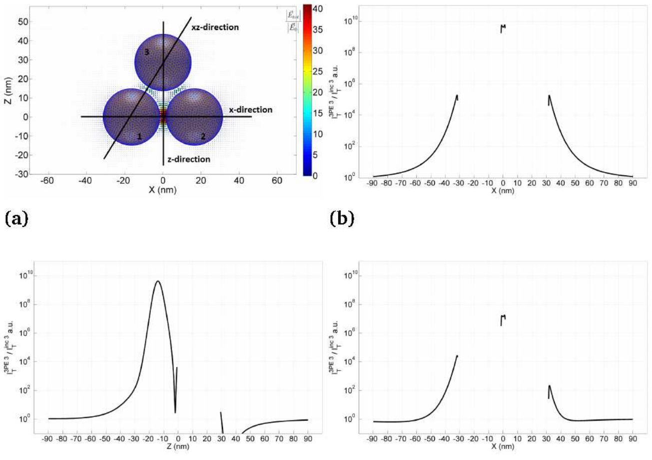

(a) (b)

(c) (d)

Fig. 9 Total electric field ($\vec{E}_{tot}$) and EM field intensity between the three NPs arranged as fixed on the tips of an equilateral triangle. The distance between NP surfaces is 3nm. Panel (a): xz view of the electric field. The colorscale and the size of the arrows represent the module of the field in unit of the incident field module ($|\vec{E}_0|$). Panels (b), (c) and (d): Third power of the total EM field intensity along the x, the z and the xz-direction, respectively. The missing parts in the plots correspond to the regions internal to the NPs.

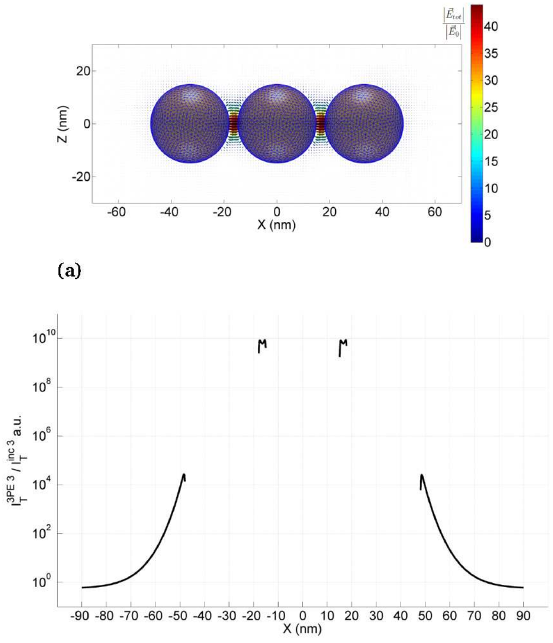

(a)

(b)

Fig. 10 Total electric field ($\vec{E}_{tot}$) and EM field intensity between the three NPs arranged in a row. The distance between NP surfaces is 3nm. Panel (a): xz view of the electric field. The colorscale and the size of the arrows represent the module of the field in unit of the incident field module ($|\vec{E}_0|$). Panel (b): Third power of the total EM field intensity along the x-direction. The missing parts in the plot correspond to the regions internal to the NPs.

To verify whether a larger aggregate can provide a greater EM field enhancement, we simulated systems of three identical nanoparticles arranged in two different configurations. Firstly, we studied the system with the particles arranged as an equilateral triangle, with two of them (NP 1 and 2) aligned in the x-direction (see Figure 9). From the plot of the electric field in the xz plane of Figure 9, the greatest enhancement takes place in the intermediate region between the these two NPs. Overall, however, this enhancement is smaller than the two NP case (Figure 9). Moreover, we note that the electric field near the middle point between the three nanoparticles is quenched: if, assuming a first-order approximation, we replace the three spheres with three dipoles oriented along the electric field and oscillating in phase, it is straightforward to realize that in the middle region the direction of the electric field produced by NP 1 and 2 is concordant, whereas the electric field by NP 3 is opposed to them resulting in a destructive interference.

Finally, we simulated a system of three identical gold nanoparticles with radius 15nm and aligned along the electric field direction (x-axis, see Figure 10). Even though we observe an enhanced EM field intensity in the intervening regions between the NPs, as we expected given the symmetry of the system, the enhancement seems still smaller than in the two NP case.

4.2.4 Electromagnetic field enhancement in aggregates of nanoparticles

From Figure 5 we can infer that the nanoparticles can be found also as aggregates. To shed light on the effect of the NP aggregation on the achievable EM field intensity enhancement, we calculated the polarization of the nanoparticles composing differently shaped aggregates. The NP polarization ($\vec{P}_{tot}$) is obtained by means of the Coupled Dipole Approximation (CDA) detailed in the "Computational details" Section. We recall that, even if the implemented interaction includes retarded effects, this method accounts only for the dipole response of the nanoparticles. It is well-known that when the distance between two NPs is less than their size (but larger than a few nanometers, so as to avoid non-local[22] and quantum effects[24,63]) multipolar contributions start being significant[64]. However, in light of the previous simulations on dimer and trimer configurations, in which the dipolar behavior turns out to be predominant, we assumed that the multipolar momenta could affect the total NP response only slightly in our case.

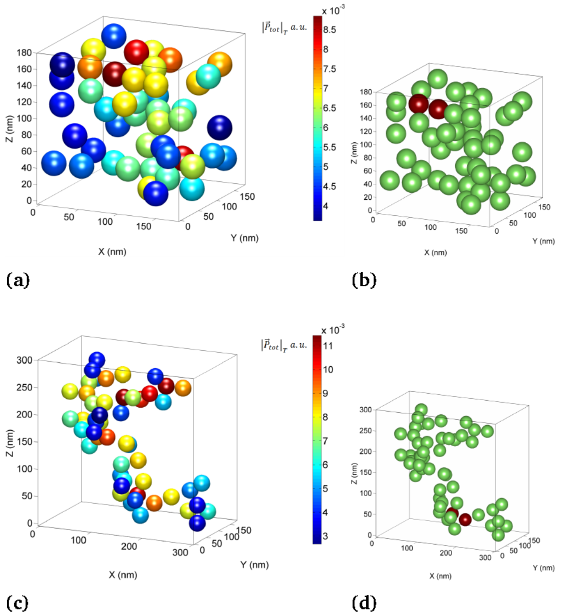

(a) (b)

(c) (d)

Fig. 11 Sphere polarization module ($|\vec{P}^{agg}_{tot}|$) and position of the selected dimer inside two diverse aggregates. Panel (a) and (c): Polarization module averaged in time of the nanoparticles composing (a) a compact and (c) an elongate aggregate; the colorscale is in arbitrary units. Panel (b) and (d): Sketch of the two aggregates marking off (red nanoparticles) the dimer configuration selected inside (green nanoparticles) the aggregate.

Five aggregates were produced with an elongate shape and five with a more compact arrangement, in order to mimic the configurations showed by the TEM images (cfr. Figure 5). The aggregates were created via a cluster-cluster aggregation algorithm, see "Computational details" Section. For each aggregate we singled out a pair of contiguous particles aligned along the direction of the incident electric field and characterized by high values of the time-averaged polarization module ($|\vec{P}^{agg}_{tot}|$) and similar dephasing. For instance, Figure 11 shows the results for a compact and an elongate aggregate. Figures 11b and 11d mark off which dimer inside each aggregate is experiencing high values of $|\vec{P}^{agg}_{tot}|$ (cfr. Figures 11a and 11c) and same dephasing (cfr. Figures S9a and S9b in the ESI).

Subsequently, we simulated the time-averaged polarization module of the same pair of NPs when the dimer is isolated ($|\vec{P}^{dim}_{tot}|$). Since, by definition, for a linear material characterized by a dipolar response

$$\vec{P}_{tot} = \tilde{\alpha}\vec{E}_{tot} \qquad (7)$$

it is straightforward to obtain

$$\frac{|\vec{P}^{agg}_{tot}|}{|\vec{P}^{dim}_{tot}|} = \frac{|\vec{E}^{agg}_{tot}|}{|\vec{E}^{dim}_{tot}|} \qquad (8)$$

with $|\vec{E}^{agg}_{tot}|$ and $|\vec{E}^{dim}_{tot}|$ being the electric field intensity acting on the dimer within and without the aggregate, respectively. This ratio between the time-averaged polarization module of the two NPs when the dimer is embedded in an aggregate and when isolated discloses the effect of the aggregate on the EM field acting on a dimer. If this ratio is bigger than 1, it means that an enhancement additional to that already discussed for the dimer hot-spot is occurring; in contrast, if this is smaller than 1, a quenching is produced by the aggregate. In both cases, the magnitude of $|\vec{E}^{agg}_{tot}|/|\vec{E}^{dim}_{tot}|$ provides an estimation of such an enhancement/quenching. The outcomes for all the ten concerned aggregates are summarized in Table 2 (the compact and elongate aggregates $2-5$ are displayed in the "Aggregate configurations" Section in the ESI).

	$|\vec{E}^{agg}_{tot}|/|\vec{E}^{dim}_{tot}|$
Compact aggregate 1	1.149333
Compact aggregate 2	1.057894
Compact aggregate 3	0.986256
Compact aggregate 4	1.273086
Compact aggregate 5	0.846057
Elongate aggregate 1	1.210362
Elongate aggregate 2	1.387799
Elongate aggregate 3	1.102673
Elongate aggregate 4	1.254035
Elongate aggregate 5	1.104187

Table 2 This table summarizes the results obtained for all the considered compact and elongate aggregates. For each aggregate the contribution of the other NPs of the aggregate to the modification of the dimer electric field is reported through the ratio $|\vec{E}^{agg}_{tot}|/|\vec{E}^{dim}_{tot}|$.

For almost all the cases, the aggregate configuration provides an additional enhancement to the electric field of a dimer. The ratio turns out to be around 1.2 on average, leading to an increase of the value of 3PE enhancement ζ by a factor around 3 with respect to the one obtained for the dimer configuration. Nevertheless, in two cases the enhancement turns out to be quenched by the presence of other surrounding NPs (see Figures S11 and S13 in the ESI). This occurs especially for dimers located at the center of very compact aggregates, when the quenching effects are bigger because of both the shorter interparticle distance (with respect to elongate aggregates) and the fact that the dimer is completely surrounded by other NPs (as compared to configurations where the dimer is close to a side of the aggregate). The quenching ratio turns out to be even as small as 0.84, leading to a decrease of η by a factor around 2.7.

To conclude, the present study (although limited in the statistics of the considered aggregates) suggests that the aggregates can provide only a minor correction to the probability of the three-photon absorption process associated with configurations of a few NPs. Indeed, the order of magnitude of the necessary EM field intensity enhancement and, in turn, the photorelease are mainly determined by compact bunches of two and three NPs. Moreover, depending on the configuration of the aggregate (shape of the aggregate, interparticle distance in the aggregate, ...) and the position of the particle inside the aggregate, the electric field enhancement can be also smaller than the one produced by a compound of a few NPs. This confirms that the latter ones are desirable for photorelease devices based on multiphoton processes.

4.3 Third Harmonic Generation by the metal NP

We now examine the magnitude of the THG field enhancement around the NP in the simplest of the geometries investigated previously. Figure 12 reports the results of THG calculation, namely the order of magnitude of the THG efficiency around the NP, expressed relative to the third power of the incident intensity ($\eta = I_T^{THG}/I_T^{inc\,3}$). The distribution of the intensity, and thus of the electric field, resembles a dipole response and the highest values of η (around $10^{-25}\mathrm{m}^4\mathrm{W}^{-2}$) are found close to the NP surface along the polarization direction. This is reasonable in light of the small ratio (NP size)/(incident wavelength)[52] and is in accordance to the literature, where notable THG is found only for structures with size of hundreds of nanometers[31,32,41].

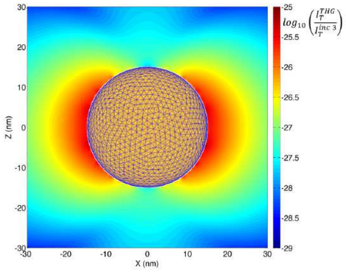

Fig. 12 *xz* view of the THG EM field intensity outside an isolated NP. The intensity is normalized to the third power of the incident intensity so that the enhancement factor f is directly obtained. The color scale represents the order of magnitude of this intensity. The incident electric field is directed along x.

We repeated the same calculation for a dimer with distance between the NP surface of 3nm. The outcomes, showed in Figure 13, reveal that the THG efficiency η around the NPs can reach values around $10^{-22}\mathrm{m}^4\mathrm{W}^{-2}$ in the hot-spot. Indeed, the NP coupling enhances the THG EM intensity around the dimer.

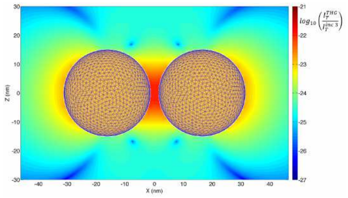

Fig. 13 *xz* view of the THG EM field intensity outside a dimer of NPs. The intensity is normalized to the third power of the incident electric field so that the enhancement factor f is directly obtained. The color scale represents the order of magnitude of this intensity.

As mentioned in the "Theory" Section, we recall that these results are obtained by using a rather conservative estimate for the THG susceptibility ($\chi^{(3)}_{3\omega} = 2.3 \cdot 10^{-18}\mathrm{m}^2/\mathrm{V}^2$), so that larger values of $\chi^{(3)}_{3\omega}$ would result in higher efficiency.

4.4 Comparison between 3PE and THG

Substitution of the values of the cross sections and the excitation energy into Equation (1) and (2) allows us to compare the effectiveness of the two possible excitation mechanisms, leading to

$$\frac{k^{THG}}{k^{3PE}} \simeq 1.7 \cdot 10^{36}\mathrm{W}^2\mathrm{m}^{-4}\,\frac{\eta}{\zeta} \qquad (9)$$

implying that THG dominates over 3PE as long as $\eta/\zeta > 10^{-36}\mathrm{m}^4\mathrm{W}^{-2}$. In the present case estimates for ζ and η in the hot-spots yield 10^{10} and $10^{-22}\mathrm{m}^4\mathrm{W}^{-2}$, respectively, so this ratio is $\approx 10^{-32}\mathrm{m}^4\mathrm{W}^{-2}$, indicating that the THG mechanism prevails.

In the dimer hot spots, at an intensity of $I^{inc} = 0.47 \cdot 10^9\mathrm{W/m}^2$ (i.e., $E_{inc} = 4.2 \cdot 10^5\mathrm{V/m}$)

$$k^{THG} = 0.61 \cdot 10^2\mathrm{s}^{-1} \qquad (10)$$

which is in the experimentally relevant range, giving release time in the ms timescale, while the 3PE excitation rate reads

$$k^{3PE} = 0.35 \cdot 10^{-2}\mathrm{s}^{-1} \qquad (11)$$

that is a borderline value.

For a single NP $\zeta \approx 4 \cdot 10^4$ and $\eta \approx 10^{-25}\mathrm{m}^4\mathrm{W}^{-2}$. Again THG prevails though the excitation rate of $k^{THG} \approx 10^{-2}\mathrm{s}^{-1}$ is only barely sufficient to trigger a relevant payload release. As such, the presence of plasmonic hot-spots seems to be necessary for an effective release.

5 Conclusions

We numerically simulated the electric field outside gold nanoparticles both isolated or interacting in clusters. These calculations provide insights on the possible mechanisms ruling the experimentally observed photocleavage occurring in AuNP-peptide-triazole-payload structures. The excitation wavelength at 561nm compared with triazole absorption at 190-200nm and the observed cubic dependence of photorelease on the EM field intensity indicate either a (three-photon) excitation by 3PE or (one-photon) excitation by THG as possible mechanisms for triazole photocleavage. Both mechanisms rely on the optical response of the NP at the plasmonic peak.

The Molecular Dynamic simulations indicate that the payload molecules, thus the photocleavable bond, are located 1-2nm far from the NP surface. Thereby, the focus is on the EM field enhancement and THG generation at that distance from the gold NP surface.

Our EM field calculations reveal that, taking into account triazole cross sections for the two processes, the THG mechanism prevails over 3PE by around three orders of magnitude in the estimated excitation rates. We find that a payload release rate compatible with the experimental findings is possible by the THG mechanism; however, this is the case only for coupled nanoparticles in contact with each other via the peptide layer (surface distance lower than 3nm). Moreover, the spatial region where it can occur is restricted to the intermediate region between the NPs and the release is only yielded when the nanoparticles are aligned along the direction of the incident electric field. In this regions the enhancement factors for the 3PE and THG process are respectively $\zeta = 10^{10}$ and $\eta = 10^{-22}\mathrm{m}^4\mathrm{W}^{-2}$, leading to excitation rates of $k^{3PE} = 0.35 \cdot 10^{-2}\mathrm{s}^{-1}$ and $k^{THG} = 0.61 \cdot 10^{2}\mathrm{s}^{-1}$: the former appears to be insufficient for an effective payload liberation, whereas the latter resides in the relevant experimental range. Clearly, a certain degree of mobility of the NPs during the irradiation time needs to be assumed in order to span several regions of the NP surface. Alternatively, deviation from the spherical shape such as the presence of sharp edges or tips may account for larger enhancements. In the absence of more precise experimental characterization we limited our analysis to the general case of perfect spheres, referring extension to different shapes to future work.

For 3PE, we have also explored NP aggregates larger than the dimer, coherently with *in vitro* results, to verify whether sufficient enhancement can be achieved also for this process. Our calculations reveal that, counterintuitively, the EM field enhancement does not rise proportionally to the increase of the nanoparticle number in the system. In fact, the multiparticle interaction may result in smaller enhancements, as in the case of three NPs systems as compared to the two NPs system. For even larger nanoparticle aggregates EM field enhancements in the hot spots are only marginally larger or, in some cases, smaller than those obtained for dimers.

In summary, the present study provides a theoretical characterization of the most effective NPs conformation in order to improve the rate of release. Based on this characterization, we could identify design principles for these systems. Firstly, the predominant activation mechanism is THG, which turns out to be more effective than the 3PE. The practical goal is thus to maximize this kind of non-linearity, rather than improving the three-photon cross section of the photo-cleavable moiety. Moreover, the results show that configurations exhibiting hot-spots are required to enable the photo-release process; however there is no benefit on the field enhancement in having aggregates larger than just a dimer. This finding can be useful for efficiently engineering the nanoparticles in the realization of new medical tools for target therapy. It is noticeable that the observation of this peculiar non-linear process opens up the study on the widely unexplored field of optical synergy within metallic nanostructures and UV-cleavable molecules.

6 Acknowledgments

The authors thank Paolo Faraci for providing the cell cultures. SC acknowledges funding from CNR Flagship project Nanomax (grant Nanobrain) and MIUR PRIN project 2012A7LMS_003.

7 TOC

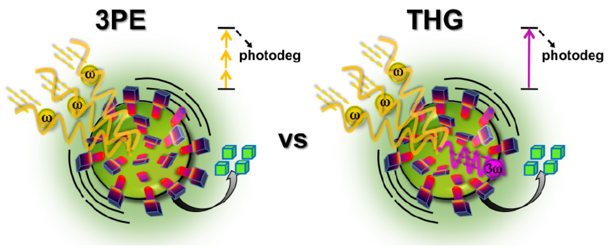

Light-triggered release of payload molecules from functionalized metal nanoparticles is achieved by photocleaving a molecular bridge via molecular absorption of plasmon-assisted non-linearly generated light.

References

1. C. Louis and O. Pluchery, *Gold Nanoparticles for Physics, Chemistry and Biology*, Imperial College Press, London, UK, 2012.
2. S. D. Brown, P. Nativo, J.-A. Smith, D. Stirling, P. R. Edwards, B. Venugopal, D. J. Flint, J. A. Plumb, D. Graham and N. J. Wheate, *J. Am. Chem. Soc.*, 2010, **132**, 4678–4684.
3. S. R. Sershen, S. L. Westcott, N. J. Halas and J. L. West, *J. Biomed. Mater. Res.*, 2000, **51**, 293–298.
4. C.-J. Carling, F. Nourmohammadian, J.-C. Boyer and N. R. Branda, *Angew. Chem. Int. Ed.*, 2010, **49**, 3782–3785.
5. R. Langer, *Science*, 2001, **293**, 58–59.
6. R. Hong, G. Han, J. M. Fernández, B.-J. Kim, N. S. Forbes and V. M. Rotello, *J. Am. Chem. Soc.*, 2006, **128**, 1078–1079.
7. V. Voliani, G. Signore, O. Vittorio, P. Faraci, S. Luin, J. Peréz-Prieto and F. Beltram, *J. Mater. Chem. B*, 2013, **1**, 4225–4230.
8. T. M. Allen and P. R. Cullis, *Science*, 2004, **303**, 1818–1822.
9. U. Kreibig and M. Vollmer, *Optical Properties of Metal Clusters*, Springer, New York, NY, 1995.
10. S. A. Maier, *Plasmonics: Fundamentals and Applications*, Springer, New York, NY, 2007.
11. V. Voliani, F. Ricci, G. Signore, R. Nifosì, S. Luin and F. Beltram, *Small*, 2011, **7**, 3271–3275.
12. V. Voliani, S. Luin, F. Ricci and F. Beltram, *Nanoscale*, 2010, **2**, 2783–2789.
13. E. M. Burgess, R. Carithers and L. McCullagh, *J. Am. Chem. Soc.*, 1968, **90**, 1923–1924.
14. I. Cohanoschi and F. E. Hernández, *J. Phys. Chem. B*, 2005, **109**, 14506–14512.
15. Y. Luo, D. Y. Lei, S. A. Maier and J. B. Pendry, *ACS Nano*, 2012, **6**, 6492–6506.
16. A. I. Fernandez-Dominguez, Y. Luo, A. Wiener, J. B. Pendry and S. A. Maier, *Nano Lett.*, 2012, **12**, 5946–5953.
17. A. Aubry, D. Y. Lei, S. A. Maier and J. B. Pendry, *Phys. Rev. Lett.*, 2010, **105**, 233901–4.

18 A. I. Fernandez-Dominguez, A. Wiener, F. J. Garcia-Vidal, S. A. Maier and J. B. Pendry, *Phys. Rev. Lett.*, 2012, **108**, 106802–5.

19 A. Aubry, D. Y. Lei, A. I. Fernandez-Dominguez, Y. Sonnefraud, S. A. Maier and J. B. Pendry, *Nano Lett.*, 2010, **10**, 2574–2579.

20 A. Aubry, D. Y. Lei, S. A. Maier and J. B. Pendry, *ACS Nano*, 2011, **5**, 3293–3308.

21 R. Esteban, A. G. Borisov, P. Nordlander and J. Aizpurua, *Nature Comm.*, 2012, **3**, 825–9.

22 D. C. Marinica, A. K. Kazansky, P. Nordlander, J. Aizpurua and A. G. Borisov, *Nano Lett.*, 2012, **12**, 1333–1339.

23 J. Zuloaga, E. Prodan and P. Nordlander, *Nano Lett.*, 2009, **9**, 887–891.

24 T. V. Teperik, P. Nordlander, J. Aizpurua and A. G. Borisov, *Opt. Express*, 2013, **21**, 27306–27325.

25 J. B. Pendry, A. Aubry, D. R. Smith and S. A. Maier, *Science*, 2012, **337**, 549–552.

26 L. Novotny and B. Hecht, *Principles of Nano-Optics*, Cambridge University Press, Cambridge, UK, 2006.

27 F. Della Sala and S. D'Agostino, *Handbook of Molecular Plasmonics*, CRC Press, Boca Raton, FL, 2013.

28 R. W. Boyd, *Nonlinear optics*, Academic Press, San Diego, CA, 3rd edn, 2008.

29 M. Agio and A. Alù, *Optical Antennas*, Cambridge University Press, Cambridge, UK, 2013.

30 M. Kauranen and A. V. Zayats, *Nat. Photonics*, 2012, **6**, 737–748.

31 M. Scalora, M. Vincenti, D. De Ceglia, V. Roppo, M. Centini, N. Akozbek and M. Bloemer, *Phys. Rev. A*, 2010, **82**, 043828.

32 M. Sivis, M. Duwe, B. Abel and C. Ropers, *Nat. Phys.*, 2013, **9**, 304–309.

33 S. A. Maier, M. L. Brongersma, P. G. Kik and H. A. Atwater, *Phys. Rev. B*, 2002, **65**, 193408–4.

34 S. Zou and G. C. Schatz, *J. Chem. Phys.*, 2004, **121**, 12606–12612.

35 L. Sweatlock, S. Maier, H. Atwater, J. Penninkhof and A. Polman, *Phys. Rev. B*, 2005, **71**, 235408–7.

36 Z. Wang, B. Lukýanchuk, W. Guo, S. Edwardson, D. Whitehead, L. Li, Z. Liu and K. Watkins, *J. Chem. Phys.*, 2008, **128**, 094705.

37 M. H. Palmer, S. V. Hoffmann, N. C. Jones, A. R. Head and D. L. Lichtenberger, *J. Chem. Phys.*, 2011, **134**, 084309.

38 L. Bergamini and S. Corni, *J. Phys. Chem. C*, 2013, **117**, 14742–14750.

39 G. Bruno, F. Babudri, A. Operamolla, G. V. Bianco, M. Losurdo, M. M. Giangregorio, O. Hassan Omar, F. Mavelli, G. M. Farinola, P. Capezzuto and F. Naso, *Langmuir*, 2010, **26**, 8430–8440.

40 M. Lippitz, M. A. van Dijk and M. Orrit, *Nano Lett.*, 2005, **5**, 799–802.

41 C. Ciracì, M. Scalora and D. R. Smith, *arXiv preprint arXiv:1311.3194*, 2013, **7**, 1–4.

42 R. W. Boyd, Z. Shi and I. De Leon, *Opt. Commun.*, 2014, **326**, 74–79.

43 M. J. A. de Dood, *Second-Harmonic Generation*, Huygens laboratorium 909a technical report, 2006.

44 F. Iori, R. Di Felice, E. Molinari and S. Corni, *J. Comp. Chem.*, 2009, **30**, 1465–1476.

45 D. Van Der Spoel, E. Lindahl, B. Hess, G. Groenhof, A. E. Mark and H. J. Berendsen, *J. Comp. Chem.*, 2005, **26**, 1701–1718.

46 D. J. Evans and B. L. Holian, *J. Chem. Phys.*, 1985, **83**, 4069–4074.

47 S. Miyamoto and P. A. Kollman, *J. Comp. Chem.*, 1992, **13**, 952–962.

48 N. Ida, *Numerical Modeling for Electromagnetic Non-Destructive Evaluation*, Chapman & Hall, New York, NY, 1995.

49 U. Hohenester and A. Trügler, *Comput. Phys. Commun.*, 2012, **183**, 370–381.

50 F. J. Garcìa de Abajo and A. Howie, *Phys. Rev. Lett.*, 1998, **80**, 5180–5183.

51 P. B. Johnson and R. W. Christy, *Phys. Rev. B*, 1972, **6**, 4370–4379.

52 C. F. Bohren and D. R. Huffman, *Absorption and Scattering of Light by Small Particles*, John Wiley & Sons, Inc, New York, NY, 1983.

53 V. Markel, *J. Mod. Optic.*, 1993, **40**, 2281–2291.

54 B. T. Draine and P. J. Flatau, *J. Opt. Soc. Am. A*, 1994, **11**, 1491–1499.

55 S. Corni and J. Tomasi, *J. Chem. Phys.*, 2002, **116**, 1156–1164.

56 V. Tamás, *Fractal Growth Phenomena*, World Scientific, Singapore, SG, 2nd edn, 1992.

57 S. Del Turco, G. Ciofani, V. Cappello, M. Gemmi, T. Cervelli, C. Saponaro, S. Nitti, B. Mazzolai, G. Basta and V. Mattoli, *Colloids Surf B Biointerfaces*, 2013, **111**, 142–149.

58 S. Vukovic, S. Corni and B. Mennucci, *J. Phys. Chem. C*, 2009, **113**, 121–133.

59 Q. Zhang, N. Large, P. Nordlander and H. Wang, *J. Phys. Chem. Lett.*, 2014, **5**, 370–374.

60 M. G. Blaber and G. C. Schatz, *Chem. Commun.*, 2011, **47**, 3769–3771.

61 T. Teperik, P. Nordlander, J. Aizpurua and A. Borisov, *Phys. Rev. Lett.*, 2013, **110**, 263901.

62 K. J. Savage, M. M. Hawkeye, R. Esteban, A. G. Borisov, J. Aizpurua and J. J. Baumberg, *Nature*, 2012, **491**, 574–577.

63 N. Zabala, E. Ogando, A. Rivacoba and F. G. de Abajo, *Phys. Rev. B*, 2001, **64**, 205410–10.

64 L. Zhao, K. L. Kelly and G. C. Schatz, *J. Phys. Chem. B*, 2003, **107**, 7343–7350.